ChemPubSoc Europe

DOI: 10.1002/ejic.201700895

EurJIC European Journal of Inorganic Chemistry

Full Paper

Nitrosyl Chemistry

CLUSTER ISSUE

Comparison of Carbazole and Fluorene Donating Effects on the Two-Photon Absorption and Nitric Oxide Photorelease Capabilities of a Ruthenium–Nitrosyl Complex

Alejandro Enriquez-Cabrera,[a,b] Pascal G. Lacroix,*[a] Isabelle Sasaki,[a] Sonia Mallet-Ladeira,[a] Norberto Farfán,[b] Rodrigo M. Barba-Barba,[c] Gabriel Ramos-Ortiz,[c] and Isabelle Malfant*[a]

Abstract: A ruthenium–nitrosyl derivative of formula $[Ru^{II}(CzT)(bipy)(NO)](PF_6)_3$ [CzT = 4′-(*N*-ethylcarbazol-3-yl)-2,2′:6′,2″-terpyridine, bipy = 2,2′-bipyridine] has been synthesized and fully characterized, and compared with the previously reported $[Ru^{II}(FT)(bipy)(NO)](PF_6)_3$ complex [FT = 4′-(9,9-dihexyl-9*H*-fluoren-2-yl)-2,2′:6′,2″-terpyridine]. Additionally, the X-ray crystal structure of $[Ru^{II}(CzT)(bipy)(NO_2)](PF_6)$, the precursor of $[Ru^{II}(CzT)(bipy)(NO)](PF_6)_3$, is reported. The presence of a tertiary amine in the carbazole unit leads to redshifted charge-transfer transitions towards the electron-withdrawing Ru–NO fragment and hence enhanced two-photon absorption (TPA) properties. In contrast, the quantum yield of the NO· photorelease process is lower for the carbazole-containing complex. The issue of optimization of the TPA versus NO·-release capabilities is addressed.

Introduction

Nitric oxide (NO·) is a highly reactive radical naturally produced by nitric oxide synthase (NOS), which plays a key role in various physiological processes such as blood regulation, immune response, neurotransmission, and respiration as well as cytotoxic activity in tumor cells by apoptosis.[1,2] However, at concentrations other than its physiological level, NO· can induce various cardiovascular, neurological, and pulmonary diseases as well as atherosclerosis and cancer.[3–5] In this context, there has been increasing interest in investigating exogenous donors capable of releasing NO· locally and quantitatively. Among them, ruthenium–nitrosyl complexes have been recognized as the most promising candidates in relation to their generally low toxicity, good stability, and ability to release exclusively NO· under light irradiation,[6] taking advantage of the noninvasive and highly controllable characteristics of light. Additionally, although most NO· donors require to be irradiated in the 300–500 nm domain, the use of the two-photon absorption (TPA) technique,[7–11] in which the molecules simultaneously absorb two photons instead of one, allows the use of optical radiation at the double of wavelength, that is, the 600–1200 nm therapeutic window of relative transparency of biological media.[12] Owing to these appealing perspectives, the issue of designing ruthenium–nitrosyl complexes exhibiting sizeable TPA capabilities is naturally being addressed.

We have recently reported on ruthenium–nitrosyl complexes constructed from 4′-(2-fluorenyl)-2,2′:6′,2″-terpyridine ligands that are capable of releasing NO· with good quantum yields upon irradiation at λ = 405 nm.[13] In these compounds, an electron-rich fluorenyl unit has been attached to the terpyridine ligand owing to the widely reported ability of fluorene to enhance the TPA properties of molecules.[14–17] Our best result obtained by this approach was provided by the $[Ru^{II}(FT)(bipy)(NO)]^{3+}$ complex {[**1**]$^{3+}$ in Scheme 1; bipy = 2,2′-bipyridine, FT = 4′-(9,9-dihexyl-9*H*-fluoren-2-yl)-2,2′:6′,2″-terpyridine}, in which two additional hexyl chains were introduced into the ligand to increase the solubility. The TPA capability of [**1**]$^{3+}$, expressed as its molecular cross-section (σ_{TPA}), was found to be equal to 108 ± 18 GM, a value probably far from being optimal. Indeed, it has been shown that increasing the "push–pull" character of the π-conjugated skeleton usually leads to an increase in σ_{TPA} in dipolar molecules.[7–11] Therefore, the idea of replacing the fluorenyl unit by a more donating fragment arises naturally.

In the present contribution, we report on the new $[Ru^{II}(CzT)(bipy)(NO)]^{3+}$ complex {[**2**]$^{3+}$ in Scheme 1; CzT = 4′-(*N*-ethylcarbazol-3-yl)-2,2′:6′,2″-terpyridine}, a chromophore related to [**1**]$^{3+}$ in which the slightly electron-donating 9,9-dihexyl-9*H*-fluorene unit is replaced by 9-ethylcarbazole, which incorporates a tertiary amine that is conjugated within the three-cycle structure with the expected outcome of an enhanced push–pull effect directed towards the withdrawing Ru(NO) unit and hence a better TPA response. After describing

[a] CNRS, Laboratoire de Chimie de Coordination (LCC), 205 route de Narbonne, BP44099, 31077 Toulouse Cedex 4, France
E-mail: pascal.lacroix@lcc-toulouse.fr
isabelle.malfant@lcc-toulouse.fr
https://www.lcc-toulouse.fr/auteur137.html
[b] Facultad de Quimica, Departamento de Quimica Orgánica, Universidad Nacional Autónoma de México, 04510 México D.F., México
[c] Centro de Investigaciones en Óptica (CIO), A.P. 1-948, 37000 León, Gto, México

Supporting information for this article is available on the WWW under https://doi.org/10.1002/ejic.201700895.

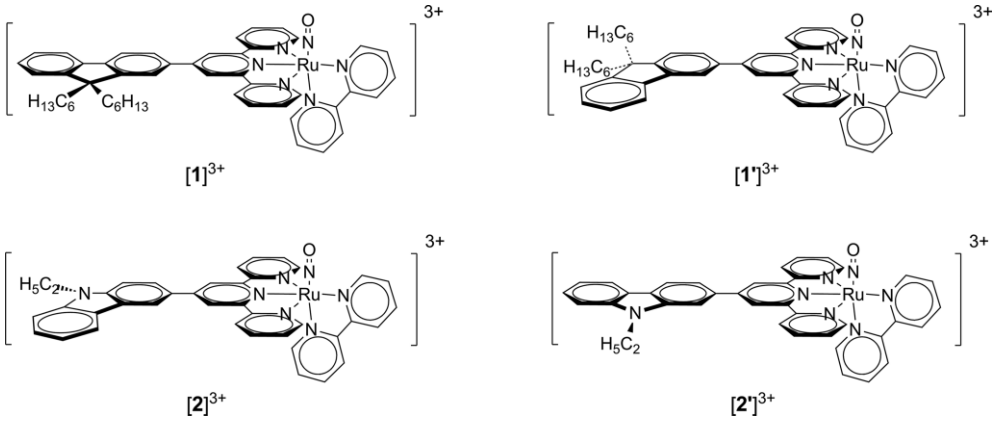

Scheme 1. Molecular formula of the four ruthenium–nitrosyl complexes under investigation.

the synthesis and characterization of $[\mathbf{2}](PF_6)_3$, its spectroscopic and photochemical properties are compared with those of the parent $[\mathbf{1}](PF_6)_3$ derivative. The observed differences have been analyzed computationally within the framework of time-dependent density functional theory (TD-DFT), which was also applied to $[\mathbf{1}']^{3+}$ and $[\mathbf{2}']^{3+}$, isomers of $[\mathbf{1}]^{3+}$ and $[\mathbf{2}]^{3+}$, to fully evaluate the capabilities of fluorene and carbazole to behave as electron donors towards a withdrawing fragment present at the 2- and 3-positions of the phenyl ring of the donor. Finally, the capabilities of the carbazole-containing $[Ru^{II}(terpy)(bipy)(NO)]^{3+}$ with respect to both efficient NO· release and TPA are critically evaluated.

Results and Discussion

Synthesis and Characterization

We have previously reported on various synthetic approaches towards ruthenium–nitrosyl complexes constructed from terpyridine ligands with the aim of avoiding 1) the formation of

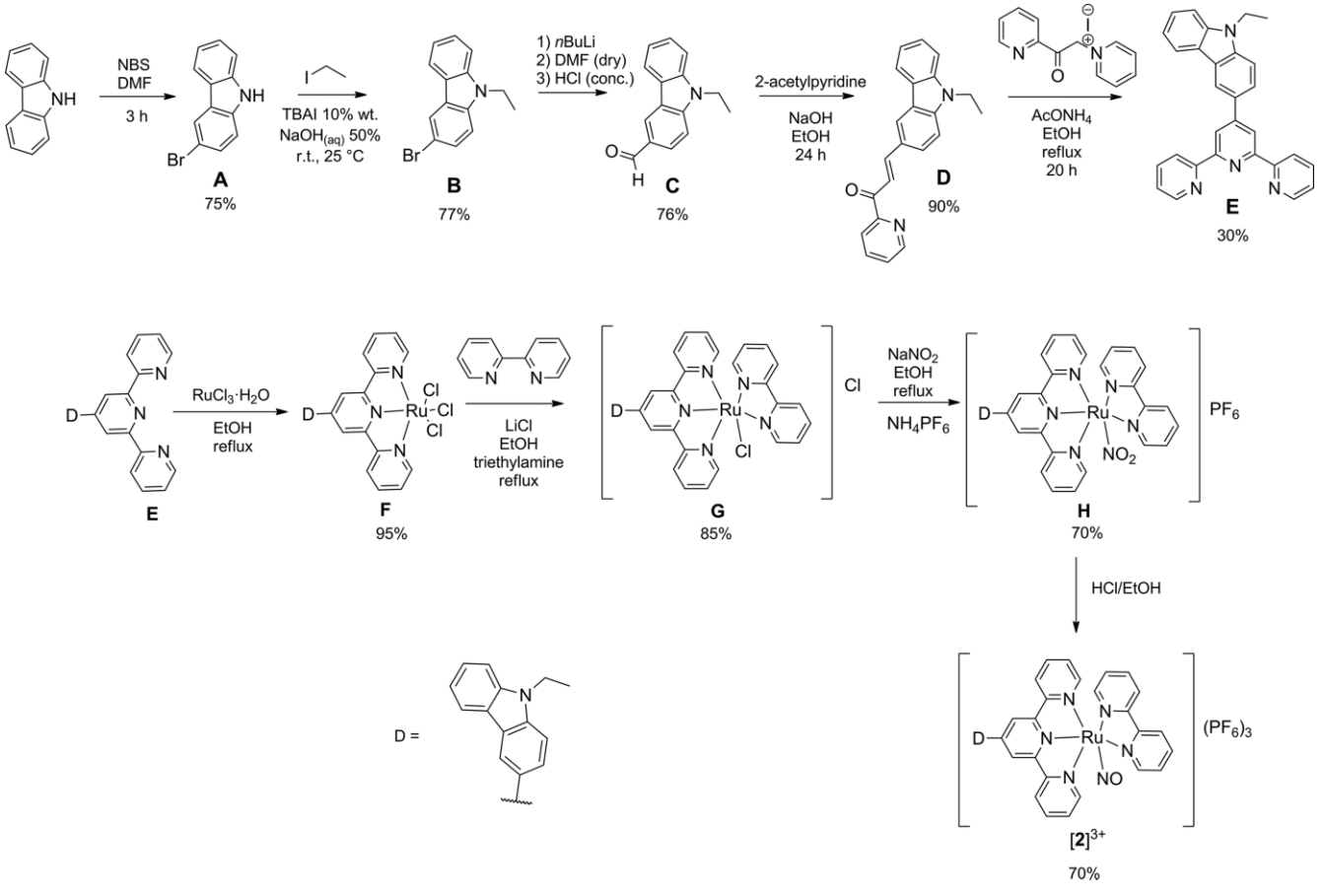

Scheme 2. Synthetic route towards ligand **E** (top) and the ruthenium–nitrosyl complex $[\mathbf{2}](PF_6)_3$ (bottom).

undesirable $[Ru^{II}(terpyridine)_2]^{2+}$ homoleptic species[13b] and 2) the tedious purification step required to separate the *trans*/*cis* isomers when two chlorides are present as ligands in the coordination sphere of the ruthenium center.[13a] The general route employed in the present investigation for the synthesis of $[\mathbf{2}](PF_6)_3$ is shown in Scheme 2, which involves first the synthesis of the 4′-(*N*-ethylcarbazol-3-yl)-2,2′:6′,2″-terpyridine ligand (**E**).

Ligand **E** was obtained in a similar manner to the fluorene derivatives[13] previously reported, using a modification of the previously reported method.[18] Its synthesis involved first brominating the carbazole by using DMF as solvent, after which alkylation was performed by a novel methodology[19] involving water, sodium hydroxide, and a phase-transfer catalyst (tetrabutylammonium iodide) at 30 °C with vigorous stirring for 24 h resulting in the pure product **B** after recrystallization. This approach avoided the use of organic solvents like DMF that are normally used for the alkylation of carbazole as well as the harsh reagent NaH.[20] The preparation of *N*-ethylcarbazole-3-carbaldehyde (**C**) and subsequent condensation with 2-acetylpyridine in basic medium resulted in the product (*E*)-3-(9-ethyl-9*H*-carbazol-3-yl)-1-(pyridin-2-yl)prop-2-en-1-one (**D**). The ligand **E** was obtained by Kröhnke condensation between **D** and the Kröhnke salt 1-(2-oxo-2-pyridin-2-ylethyl)pyridinium iodide. Note, if hexyl chains had been used instead of ethyl chains, the products **B** and **C** would have been oils requiring purification by column chromatography.

The procedures followed to obtain the different complexes were the same as for the previously reported fluorene-based complexes.[13a] First, treating ligand **E** with 1 equiv. of $RuCl_3$ in ethanol resulted in complex **F**, which was treated with 2,2′-bipyridine in the presence of an excess of LiCl and triethylamine as reducing agent to give complex **G**. By using sodium nitrite, the chloride ligand was replaced by a nitro ligand to yield complex **H**, and finally the use of 12 M HCl led to the metathesis of the nitro ligand to the nitrosyl moiety to give the desired complex $[\mathbf{2}](PF_6)_3$.

During the course of the synthesis a qualitative exploration of the colors of the products (either in solution or in the solid state) suggested that the reaction was completed, because **F** is brown, **G** is purple, **H** is red, and the final nitrosyl complex $[\mathbf{2}](PF_6)_3$ is purple again. This evolution was readily confirmed by UV/Vis spectroscopic analysis, which showed that **G** (chlorido ligand) exhibits an absorption maximum at 517 nm, **H** (nitro ligand) at 490 nm, and the final $[\mathbf{2}](PF_6)_3$ at 517 nm, making it possible to follow the different reaction steps by UV/Vis spectroscopy. Additionally, ^{1}H NMR spectroscopy is a valuable tool for identifying the ligand attached to the ruthenium center due to the shift of the 6-H of the bipyridine from 10.30 to 9.95 and 9.35 ppm for the chloride (**G**), nitro (**H**), and nitrosyl ($[\mathbf{2}]^{3+}$) ligands, respectively, as illustrated in Figure 1. This shift arises due to the fact that 6-H is spatially close to the ligands Cl^-, NO_2^-, and NO^+ in the ruthenium complexes, so any substitution leads to a significant change in the chemical shift due to a

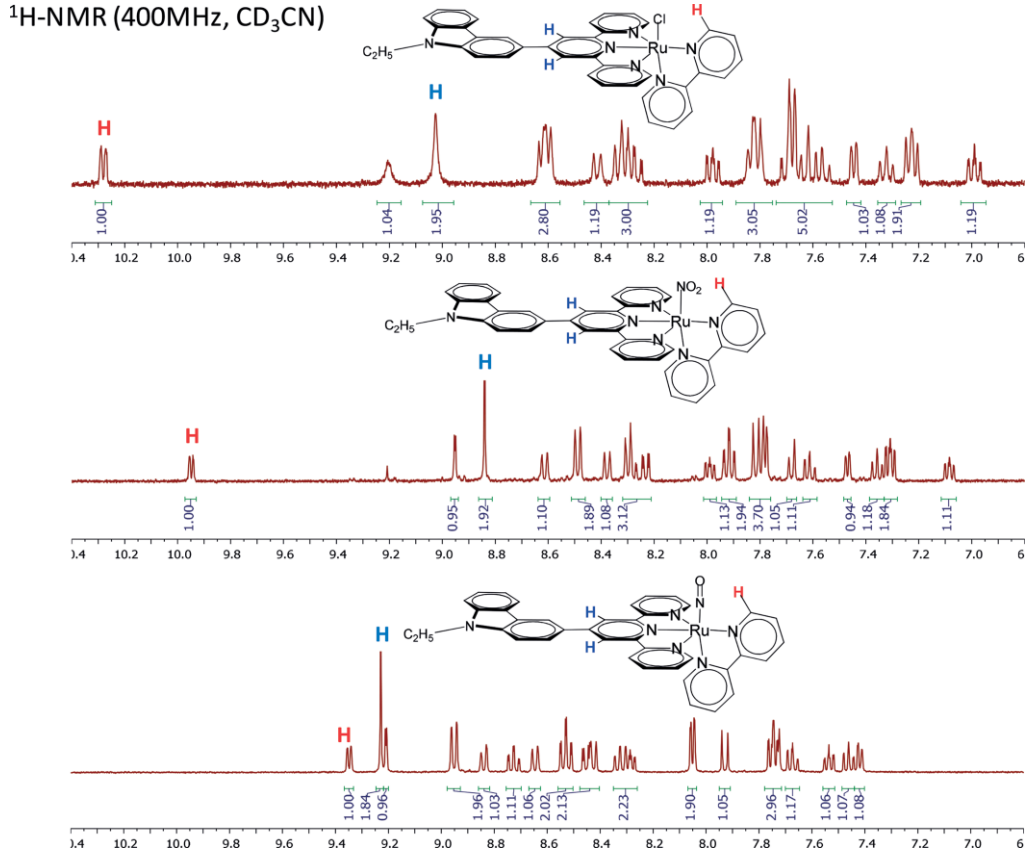

Figure 1. ^{1}H NMR spectra showing the sensitivity of the chemical shift of 6-H (in red) on going from **G** (top), to **H** (middle), and $[\mathbf{2}]^{3+}$ (bottom).

different electronic environment. The nature of the ligand (NO_2/NO) was also confirmed by IR spectroscopy through the presence of bands at 1331 and 1295 cm^{-1} (nitro) or at 1937 cm^{-1} (nitrosyl).

Structural Studies

To date, we have reported the X-ray crystal structures of three ruthenium–nitrosyl complexes constructed from fluorenylterpyridine ligands.[13] In these cases, crystals suitable for X-ray diffraction measurements were grown by slow diffusion of diethyl ether into a concentrated solution of the desired complex in acetonitrile. However, this approach failed here in the case of the carbazole-based species, which is much more difficult to crystallize despite many attempts carried out in various solvents. Nevertheless, suitable crystals of complex **H**, which contains the $Ru(NO_2)$ moiety instead of Ru(NO), were finally obtained by diffusion of diethyl ether into a concentrated solution of the complex in a 1:1 mixture of acetone/DMF.

$[Ru^{II}(bipy)(\mathbf{E})(NO_2)](PF_6)$ (**H**) crystallizes in the monoclinic $P2_1/n$ space group. The main crystal data are presented in Table 1. The overall structure results from a three-dimensional array of cationic complexes linked to each other with short contacts through $(PF_6)^-$ anionic bridges. The asymmetric unit cell, shown in Figure 2, is formed of one $[Ru^{II}(bipy)(\mathbf{E})(NO_2)](PF_6)$ entity with one molecule of DMF. Importantly, disorder appears at the NO_2^- ligand, which was successfully resolved by introducing both a nitro group and a chlorine atom in a ratio 90:10 after refinement with a Ru–Cl distance of 2.32(2) Å. This distance falls in the 2.317(3)–2.394(1) Å range of Ru–Cl bond lengths observed for our previously described $[Ru^{II}(R\text{-terpyridine})(Cl)_2(NO)](PF_6)$ complexes[21] and therefore appears to be chemically satisfactory. The unexpected presence of chlorine in the crystal structure is likely related to the fact that **H** is synthesized from complex **G**, which contains the RuCl moiety instead of $Ru(NO_2)$. The sample used for crystal growth could therefore have contained traces of the product obtained in the previous synthetic step. Additionally, the Ru–N distance in the $Ru(NO_2)$ unit is 2.009(8) Å, a rather short value but compatible with previously reported values. Indeed, 18 entries have been found in the Cambridge Structural Database containing the "Ru–terpyridine–NO_2" core. Of these, the shortest Ru–NO_2 distances are 2.013(2),[22] 2.029(2),[23,24] and 2.029(3) Å.[25]

Table 1. Crystal data and structure refinement parameters for **H**.

Chemical formula	$C_{39}H_{30}Cl_{0.1}N_{6.9}O_{1.8}Ru$, F_6P, C_3H_7NO
M_r	946.76
Crystal system	Monoclinic
Space group	$P2_1/n$
T [K]	100(2)
λ (Mo-K_α) [Å]	0.71073
a [Å]	11.6045(15)
b [Å]	14.4506(19)
c [Å]	23.486(3)
α [°]	90
β [°]	93.979(4)
γ [°]	90
V [Å^3]	3928.9(9)
Z	4
$D_{calcd.}$ [g cm^{-3}]	1.601
Absorption coefficient [mm^{-1}]	0.527
Reflections collected	68343
Unique reflections	8075
R_{int}	0.0969
R_1[a]	0.0434
wR_2[b] [$I > 2\sigma(I)$]	0.0877
(for all)	0.1010
GOF [F^2]	1.046

[a] $R_1 = \Sigma||F_o| - |F_c||/\Sigma|F_o|$. [b] $wR_2 = \{\Sigma[w(F_o^2 - F_c^2)^2]/\Sigma[w(F_o^2)^2]\}^{1/2}$.

The molecular structure of the $[Ru^{II}(bipy)(\mathbf{E})(NO_2)]^+$ cation appears less distorted than that of the previously reported $[Ru^{II}(4'\text{-fluorenylterpyridyne})(bipy)(NO)]^{3+}$ complex[13a] (non-alkylated version of $[\mathbf{1}]^{3+}$), in particular, at the terpyridine, for which the greatest deviation from the mean plane (18 atoms) is 0.143 Å, a value reduced to 0.090 Å in the present case. Addi-

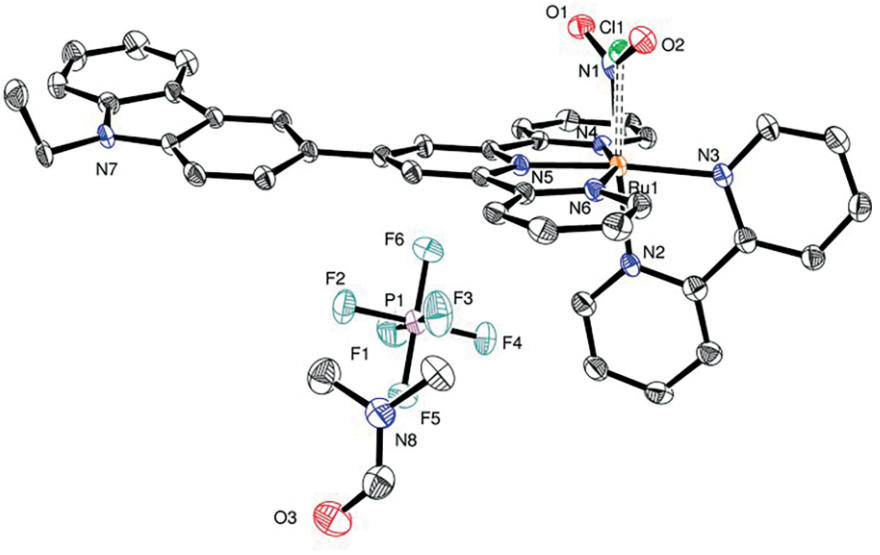

Figure 2. Asymmetric unit cell of complex **H** with the atomic labeling scheme. Displacement ellipsoids are drawn at the 50 % probability level. Hydrogen atoms have been omitted for clarity.

Table 2. Selected bond lengths and angles in complex **H** and a comparison with those of the nonalkylated $[\mathbf{1}]^{3+}$.[a]

Bond length [Å]	**H**	$[\mathbf{1}]^{3+}$	Bond angle [°]	**H**	$[\mathbf{1}]^{3+}$
Ru–N1	2.009(8)	1.762(2)	N1–Ru–N4	89.9(3)	93.13(10)
$Ru–N2_{bpy}$	2.064(3)	2.0871(19)	N1–Ru–N5	87.4(2)	98.14(9)
$Ru–N3_{bpy}$	2.087(3)	2.0931(19)	N1–Ru–N6	90.6(2)	94.91(10)
$Ru–N4_{terpy}$	2.069(3)	2.081(2)			
$Ru–N5_{terpy}$	1.965(3)	1.9814(18)	N4–Ru–N5	79.10(11)	79.79(8)
$Ru–N6_{terpy}$	2.074(3)	2.085(2)	N5–Ru–N6	79.63(12)	79.35(8)

[a] Data from ref.[13a]

tionally, the angle between the average mean planes of terpyridine and carbazole (11 atoms) is 5.55°, which indicates complete π delocalization. The coordination sphere around the ruthenium(II) atom is pseudo-octahedral; selected bond lengths and angles listed in Table 2.

The averaged data indicates a slight contraction of 0.014 Å in **H**, compared with in $[\mathbf{1}]^{3+}$, for the five Ru–N bond lengths of the ter- and bipyridine ligands. The presence of a longer Ru–N distance [2.009(8) Å] for the nitrate ligand in **H**, compared with 1.763(2) Å for the nitrosyl ligand in $[\mathbf{1}]^{3+}$, may qualitatively account for this difference. Although the position of the ruthenium atom in the vicinity of the terpyridine (N4, N5, and N6) is roughly the same for both derivatives in terms of distances and angles, a sizeable difference is observed in the position of N1, with the Ru–N1 bond nearly perpendicular to the terpyridine–ruthenium plane in **H**, in striking contrast to $[\mathbf{1}]^{3+}$, in which the Ru–NO bond is bent in the direction of the bipyridine with the N1–Ru–N4, N1–Ru–N5, and N1–Ru–N6 angles significantly larger than 90°. In contrast, the coordination sphere around the ruthenium atom of **H** exhibits a stronger octahedral character.

Although no experimental crystal data is available for ruthenium–nitrosyl complexes containing carbazole, it may be interesting to explore the donating capabilities of the different ligands on the basis of structural insights obtained by DFT computations of $[\mathbf{1}]^{3+}$, $[\mathbf{2}]^{3+}$, $[\mathbf{1'}]^{3+}$, and $[\mathbf{2'}]^{3+}$. The relevant data are presented in Table 3. In particular, the torsion angle between the averaged planes of the terpyridine and the donating (either fluorene or carbazole) substituent is a parameter of interest for evaluating the charge-transfer capabilities allowed by π-overlaps between organic fragments. It is known that the transfer integral between the π subunits, and hence the overlap integral, vary as the cosine of the torsion angle,[26] thus leading to enhanced push–pull effects towards the withdrawing nitrosyl at lower angles. Therefore it is clear from Table 3 that the structure of $[\mathbf{2}]^{3+}$ is the most favorable one in terms of the charge-transfer effect and hence TPA capabilities.

Table 3. Selected geometrical parameters in the DFT-computed structures of the $[\mathbf{1}]^{3+}$, $[\mathbf{2}]^{3+}$, $[\mathbf{1'}]^{3+}$, and $[\mathbf{2'}]^{3+}$.

	C–C bond [Å]	Torsion angle[a] [°]
$[\mathbf{1}]^{3+}$	1.467	31.28
$[\mathbf{2}]^{3+}$	1.461	28.30
$[\mathbf{1'}]^{3+}$	1.472	33.19
$[\mathbf{2'}]^{3+}$	1.467	30.77

[a] Torsion angle between the planes of the terpyridine and the donating (fluorene or carbazole) substituent.

Additionally, the frequency of the ν(NO) stretching vibration is also a good indicator of the amount of electron density transferred to the strongly withdrawing nitrosyl ligand through the well-known $Ru^{II} \rightarrow \pi^*_{NO}$ back-bonding.[6b,27] Indeed, the electron density is invariably transferred to an antibonding orbital, with the outcome being a lowering of the N–O bond order and hence a lowering of its IR stretching frequency. In the present case, the ν(NO) band can be seen at 1937 cm^{-1} in $[\mathbf{2}](PF_6)_3$, which is a slightly lower energy than the previously reported value of 1942 cm^{-1} for $[\mathbf{1}](PF_6)_3$. However, it is important to bear in mind that great care must be taken in the analysis of the shifts in energy observed for ν(NO) in the solid state. For instance, it has been reported that ruthenium–nitrosyl complexes containing terpyridine could exhibit ν(NO) bands at different frequencies, depending on the nature of the counter ion (e.g., with PF_6^-[28] and Cl^-[29]), due to different solid-state environments. Nevertheless, the data obtained from DFT computations performed on isolated cationic complexes confirm the tendency (Table 4). The lowering of 5 cm^{-1} observed in $[\mathbf{2}](PF_6)_3$ with respect to the parent $[\mathbf{1}](PF_6)_3$ compound suggests that a carbazole unit behaves as a better electron donor than a fluorene, as anticipated from the effect of its electron-rich nitrogen atom. Along this line, $[\mathbf{2}]^{3+}$ appears to be the best candidate among the series of complexes $[\mathbf{1}]^{3+}$, $[\mathbf{2}]^{3+}$, $[\mathbf{1'}]^{3+}$, and $[\mathbf{2'}]^{3+}$. Overall, the computed structural data and IR stretching frequencies correlate fairly well and suggest that the push–pull charge-transfer capability varies as follows: $[\mathbf{2}]^{3+} > [\mathbf{2'}]^{3+} \approx [\mathbf{1}]^{3+} > [\mathbf{1'}]^{3+}$.

Table 4. Experimental IR ν(NO) stretching frequencies for $[\mathbf{1}](PF_6)_3$ and $[\mathbf{2}](PF_6)_3$, and comparson with the DFT-computed values obtained for $[\mathbf{1}]^{3+}$, $[\mathbf{2}]^{3+}$, $[\mathbf{1'}]^{3+}$, and $[\mathbf{2'}]^{3+}$.

Compound	ν(NO) [cm^{-1}]	
	DFT computation	Experimental
$[\mathbf{1}]^{3+}$	2045	1942[a]
$[\mathbf{2}]^{3+}$	2039	1937[b]
$[\mathbf{1'}]^{3+}$	2048	
$[\mathbf{2'}]^{3+}$	2045	

[a] In $[\mathbf{1}](PF_6)_3$. [b] In $[\mathbf{2}](PF_6)_3$.

Spectroscopic Properties

The UV/Vis spectra of $[\mathbf{1}](PF_6)_3$ and $[\mathbf{2}](PF_6)_3$ in acetonitrile are presented in Figure 3. In both cases, complexation leads to the appearance of low-lying transitions that are absent in the related terpyridine ligands. This suggests that the Ru(NO) unit is strongly involved in these transitions, which are all potentially

active in NO· release processes. At first glance, the effect of substitution of fluorene by carbazole is that of a global redshift. More precisely, [**2**](PF$_6$)$_3$ is dominated by a low-lying intense band centered at 517 nm (ε = 14 600 L mol^{-1} cm^{-1}), which has to be compared with that of [**1**](PF$_6$)$_3$ observed at 453 nm (ε = 16 700 L mol^{-1} cm^{-1}). The sizeable shift of 64 nm is indicative of an enhancement of the push–pull effect, readily ascribed to the better donating capability of the carbazole, as discussed in the previous section.

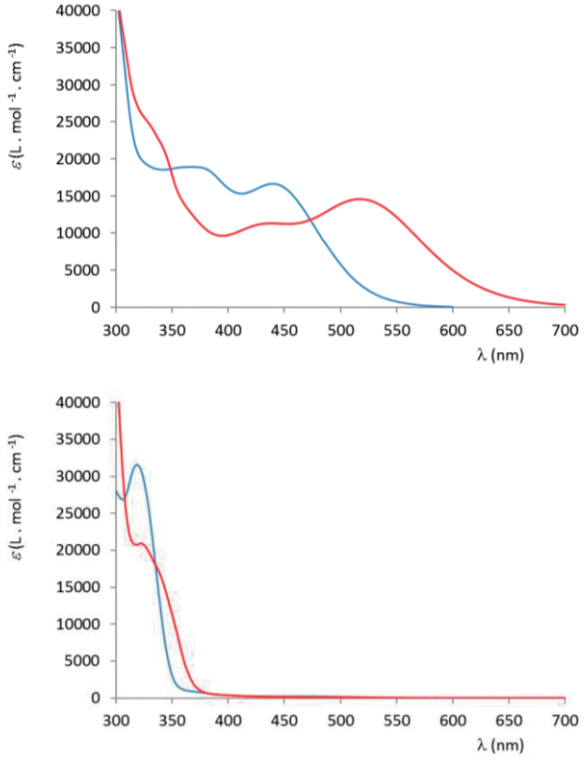

Figure 3. UV/Vis spectra of [**1**](PF$_6$)$_3$ (blue) and [**2**](PF$_6$)$_3$ (red) in acetonitrile (top), and of their corresponding terpyridine ligands (bottom).

To gain more theoretical insight into the origin and full extent of these differences, the TD-DFT-computed spectra are shown in Figure 4. The global redshift observed on going from [**1**]$^{3+}$ to [**2**]$^{3+}$ is confirmed by the calculations. Additionally, the wavelengths of the low-energy dominant transitions can be compared with the experimental values in Table 5. The slight discrepancy observed in the high-energy transition of [**2**](PF$_6$)$_3$ (380/436 nm) remains below 3500 cm^{-1}, which is still acceptable for molecules containing heavy atoms in which the transitions show a strong charge-transfer character.[30] The fair agreement between computation and UV/Vis data makes the analysis relevant at the orbital level.

The transitions involved in the electronic spectra of [**1**]$^{3+}$, [**2**]$^{3+}$, [**1′**]$^{3+}$, and [**2′**]$^{3+}$ are shown in Table 6. It is clear that the analysis of the properties at the molecular level can be restricted to a limited set of orbitals: The HOMO and LUMO for the fluorenyl derivative [**1**], and the HOMO–1 HOMO, and LUMO for the carbazole derivative [**2**]. These orbitals are shown in Figure 5. The donating character of the fluorene and carbazole

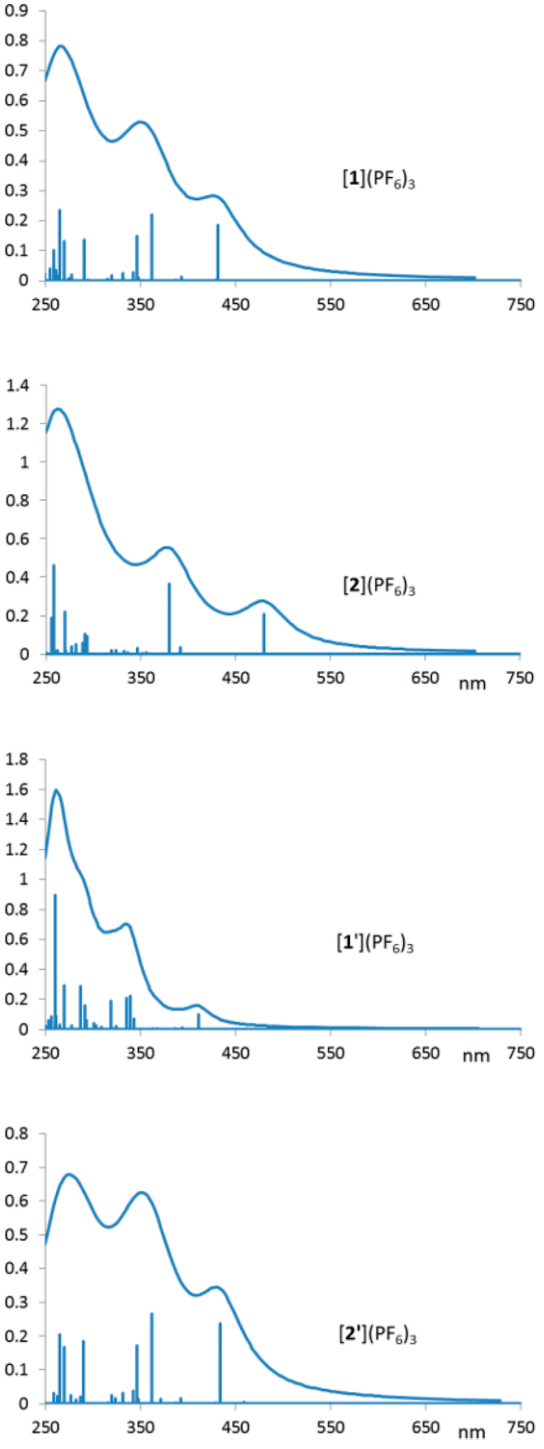

Figure 4. TD-DFT computed electronic spectra of [**1**]$^{3+}$, [**2**]$^{3+}$, [**1′**]$^{3+}$, and [**2′**]$^{3+}$.

Table 5. UV/Vis spectra and TD-DFT-computed data for [**1**](PF$_6$)$_3$ and [**2**](PF$_6$)$_3$.

	TD-DFT		UV/Vis	
	λ_{max} [nm]	f	λ_{max} [nm]	ε [M^{-1} cm^{-1}]
[**1**](PF$_6$)$_3$	432	0.336	453	16700
	363	0.398	367	18900
[**2**](PF$_6$)$_3$	480	0.297	517	14600
	380	0.522	436	11300

Table 6. Relevant TD-DFT data for the main transitions of the ruthenium complexes $[\mathbf{1}]^{3+}$, $[\mathbf{2}]^{3+}$, $[\mathbf{1'}]^{3+}$, and $[\mathbf{2'}]^{3+}$.

Compound	Transition	λ_{max}[a] [nm]	f[b]	$\Delta\mu$[c] [D]	Composition of CI expansion[d]	Character[e]
$[\mathbf{1}]^{3+}$	1→2	432	0.336	30.9	167→168 (80 %)	fluorene→Ru(NO)
	1→7	363	0.398	15.0	167→170 (34 %) + 164→169 (18 %)	fluorene-terpy→terpy-Ru(NO)
$[\mathbf{1'}]^{3+}$	1→3	411	0.091	36.3	167→168 (79 %)	fluorene→Ru(NO)
	1→10	339	0.200		164→169 (68 %) + 165→168 (16 %)	fluorene-terpy→terpy-Ru(NO)
	1→11	336	0.190		167→170 (74 %)	fluorene→terpy-Ru(NO)
$[\mathbf{2}]^{3+}$	1→2	480	0.297	27.5	167→168 (86 %)	carbazole→Ru(NO)
	1→8	380	0.522	7.70	167→170 (70 %)	carbazole→terpy-Ru(NO)
$[\mathbf{2'}]^{3+}$	1→3	434	0.337	27.9	166→168 (81 %)	carbazole→Ru(NO)
	1→10	362	0.379		166→170 (35 %) + 164→169 (17 %)	carbazole-terpy→terpy-Ru(NO)
	1→12	346	0.245		166→170 (43 %) + 164→169 (23 %)	carbazole-terpy→terpy-Ru(NO)

[a] Absorption maxima. [b] Oscillator strength. [c] Change in dipole moment ($\Delta\mu$) in the low-lying transition. [d] Composition of the configuration interaction (CI). Excitations contributing more than 15 % to the transitions. For the four compounds, orbital 167 is the HOMO and orbital 168 is the LUMO. [e] Dominant character of the charge transfer.

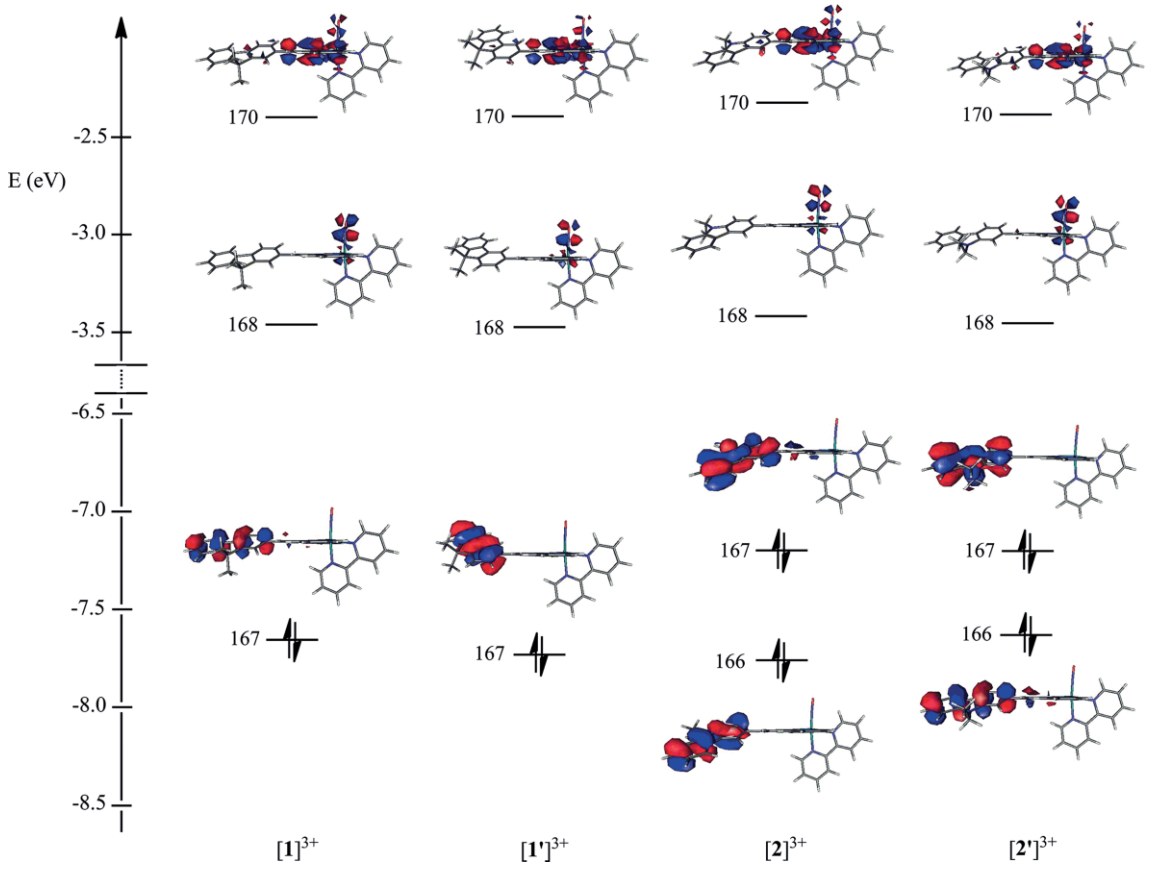

Figure 5. Main orbitals and relative energies computed by DFT for $[\mathbf{1}]^{3+}$, $[\mathbf{2}]^{3+}$, $[\mathbf{1'}]^{3+}$, and $[\mathbf{2'}]^{3+}$.

substituents and the withdrawing character of the ruthenium–nitrosyl units are clear from the orbital diagrams, as are the higher energies of the occupied levels of the carbazole, a strong indication of 1) its enhanced donating character and 2) the resulting push–pull effect expected in $[\mathbf{2}]^{3+}$.

Cyclic voltammetry experiments revealed additional features of the enhanced ligand donating capability in $[\mathbf{2}](PF_6)_3$. The redox potentials measured for $[\mathbf{1}](PF_6)_3$ and $[\mathbf{2}](PF_6)_3$ are presented in Table 7. The presence of two reduction waves in the voltammograms (see Figure S1 in the Supporting Information) is consistent with previous reports on Ru(terpy)(NO) derivatives,[31–33] and they have been ascribed to $RuNO^+ \rightarrow RuNO\cdot$ and $RuNO\cdot \rightarrow RuNO^-$ reduction processes with a potential difference of ΔE = 700 mV for each compound leading to comproportionation constants (K_c) of 0.7×10^{12} ($RT\ln K_c = \Delta E/0.059$). Slightly lower reduction potentials are observed for $[\mathbf{2}](PF_6)_3$, with an offset of 20 mV. This difference indicates the presence of a less reducible nitrosyl fragment on $[\mathbf{2}]^{3+}$, which in turn indicates an enhanced electron density on the nitrosyl and therefore an enhanced donating effect induced by the carbazole compared with that of the fluorenyl ligand. The slightly lower value of 20 mV is related to the fact that the redox features are centered

on the Ru(NO) unit with a similar environment in the two complexes. In contrast, the differences in the orbitals are more pronounced for the ligand-centered occupied levels (fluorene vs. carbazole) leading to a more sizeable shift in the absorption spectra (Figure 3).

Table 7. Electrochemical data in acetonitrile ($E^{1/2}$ vs. SCE) for [**1**](PF$_6$)$_3$ and [**2**](PF$_6$)$_3$.

Compounds	$E^{1/2}$(NO+/NO·)[a] [V]	$E^{1/2}$(NO·/NO$^-$)[b] [V]
[**1**](PF$_6$)$_3$	0.45	–0.25
[**2**](PF$_6$)$_3$	0.43	–0.27

[a] Reversible. [b] Irreversible.

TPA Properties

To quantify the TPA properties we employed the Z-scan technique (due to the absence of significant fluorescence in the ruthenium complexes, the use of other techniques such as two-photon excited fluorescence was precluded). Under the experimental conditions employed in this work, an incident wavelength of 800 nm leads to a TPA absorption at 400 nm, which does not correspond to the absorption maxima of the ruthenium complexes [453 and 517 nm for [**1**](PF$_6$)$_3$ and [**2**](PF$_6$)$_3$, respectively]. Nevertheless, and apart from the fact that two-photon electronic spectra may be significantly different to one-photon spectra, it is important to bear in mind that the 800 nm wavelength is the most widely used wavelength in biophotonics applications for practical reasons and therefore was the one selected here.

At the molecular level, the quantification of the TPA properties is expressed by a cross-section (σ_{TPA}), expressed in Göppert–Mayer units (1 GM = 10^{-50} cm^4 s photon^{-1} molecule^{-1}). By using the Z-scan technique, we measured the nonlinear absorption coefficient (β) in acetonitrile solutions of [**2**]$^{3+}$ at the concentration of 10^{-2} mol L^{-1}. Samples at high concentrations are necessary in this technique to assure that traces of transmission can be detected in the far-field region with a good signal-to-noise ratio. Figure 6 presents typical traces of the normalized transmission [$T(z)$, see the Exptl. Sect.] obtained from Z-scan experiments of samples of [**2**](PF$_6$)$_3$ contained in a 1-mm-thick quartz cuvette. The presented traces were obtained with pulse energies from 180 to 460nJ for a pulsewidth of 350 fs. It is observed that the Z-scan traces exhibit good symmetry at around $Z = 0$ and that the normalized transmission decreases as the intensity of the pulse increases. The dependence of the intensity of transmission is a distinctive feature of a nonlinear absorption process. Good fitting to the experimental data by using the mathematical formalism for the Z-scan technique[34] corroborated TPA as the origin of the nonlinear absorption shown in Figure 6. Note that multistep two-photon excitation due to the absorption of excited states is avoided because the employed IR excitation (800 nm) is far from the one-photon resonance (515 nm) and the tail of lineal absorption (see Figure 3). We also point out that despite the high intensities, no artifacts in the Z-scan traces can be detected, that is, thermo-optical effects, which usually introduce strong distortion. The Z-scan experiments were repeated several times and the mean β value for each pulse energy is displayed in the inset of Figure 6. According to these results, the β coefficient shows a negligible dependence on the energy of excitation for the range of energies employed in the Z-scan experiments. Thus, the average value of β for [**2**](PF$_6$)$_3$ and the corresponding σ_{TPA} from a total of 25 plots resulted in the values presented in Table 8, which also shows the β and σ_{TPA} values for the fluorene-based parent compound [**1**](PF$_6$)$_3$.

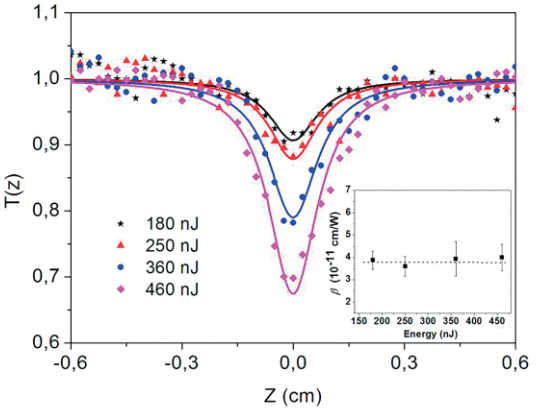

Figure 6. Normalized transmission in Z-scan experiments for [**2**](PF$_6$)$_3$ with different energies of excitation at the wavelength of 800 nm. Inset: Average values of the nonlinear absorption coefficient β as a function of energy.

Table 8. Nonlinear absorption coefficients (β) and TPA cross-sections (σ_{TPA}) for [**1**](PF$_6$)$_3$ and [**2**](PF$_6$)$_3$ at an incident laser wavelength of 800 nm.

Compound	β [10^{-11} cm W^{-1}]	σ_{TPA} [GM]	Ref.
[**2**](PF$_6$)$_3$	3.85 ± 0.55	159.2 ± 22	This work
[**1**](PF$_6$)$_3$	2.63 ± 0.43	108.0 ± 18	[13a]

The σ_{TPA} value obtained for [**2**](PF$_6$)$_3$ is 159.2 GM, which is about 1.5 times higher than that of the fluorene-based parent compound [**1**](PF$_6$)$_3$. This enhancement in TPA response is consistent with the redshift of 64 nm of the low-lying absorption band observed after the substitution of fluorene in [**1**]$^{3+}$ by carbazole in [**2**]$^{3+}$, which indicates the potential effect of the donating capability of the tertiary amine present in the carbazole moiety.

NO Release from [1](PF$_6$)$_3$ and [2](PF$_6$)$_3$

As previously reported for several ruthenium–nitrosyl complexes incorporating a fluorene-terpyridine ligand,[13] irradiation results in the release of the nitric oxide radical followed by the formation of a solvent-bound ruthenium(III) photoproduct [Equation (1)].

$$(\mathrm{L})\mathrm{Ru^{II}\text{-}NO^+} + \mathrm{solvent} \xrightarrow{h\nu} (\mathrm{L})\mathrm{Ru^{III}\text{-}solvent} + \mathrm{NO}\cdot \quad (1)$$

The efficient photoinduced release of NO· from the [**2**](PF$_6$)$_3$ complex in acetonitrile solution under standard (one-photon) excitation at 436 nm can be further demonstrated by means of EPR spectroscopy, because spin-trapping combined with EPR

spectroscopy is considered to be one of the best methods for the direct detection of NO· radicals.[35] Thus, we used *N*-methyl-D-glucamine-dithiocarbamato-iron(II) [$Fe^{II}(MGD)_2$] to trap NO· due to its high tendency to form adducts and the high stability of the spin adduct. Figure 7 shows the characteristic triplet signal with a hyperfine splitting constant of $a_N = 1.2 \times 10^{-3}$ cm^{-1} and a *g* factor of $g = 2.039$. This is consistent with the data reported in the literature for the [$Fe^{II}(MGD)_2$-NO] adduct.[36] The weak signal observed in the control spectrum (top of Figure 7) arises from a trace of NO· due to the fact that the manipulation is never strictly conducted in the dark.

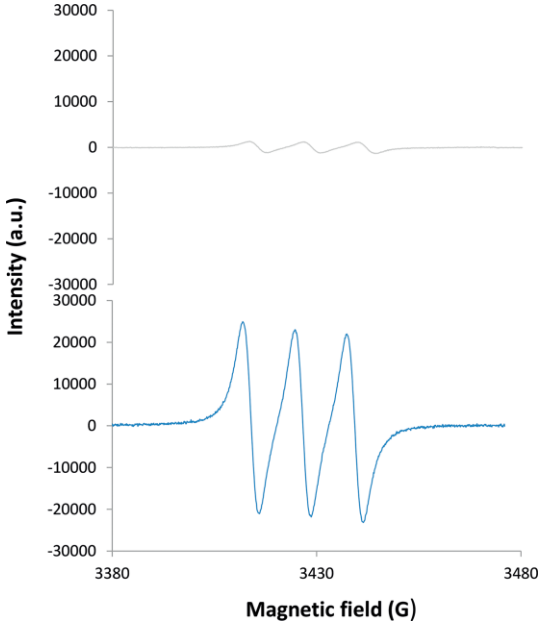

Figure 7. Triplet EPR signals from NO· released from [**2**]$(PF_6)_3$ and trapped by [$Fe(MGD)_2$] upon one-photon excitation at $\lambda > 400$ nm (Hg lamp) at room temperature (bottom) and the control signal recorded before irradiation (top).

The changes in the electronic absorption spectrum of [**2**]$(PF_6)_3$ in acetonitrile upon exposure to 436 nm light are shown in Figure 8. The presence of isosbestic points at 338, 350, 406, 426, and 496 nm indicates a clean conversion of the $Ru^{II}(NO^+)$ complexes into the corresponding photolyzed species. No back-reaction was observed when the light was turned off. For the photolyzed species, new bands located at 320, 370, and 472 nm arise. It is interesting to observe that the spectral shape of the final product (red line in Figure 8) corresponds to a Ru^{II} complex (lack of band at 600 nm characteristic of Ru^{III} species).[13c] This suggests that the photoproduct may be reduced immediately after the photoreaction, leading to a Ru^{II} complex as the final observable product. Nevertheless, the isosbestic points evidenced in Figure 8 indicate that this second step is probably extremely fast. Similar behavior was observed for [**1**]$(PF_6)_3$ (see Figure S2 in the Supporting Information). The observation of the final Ru^{II} species instead of the expected Ru^{III} species appears to be a rather general feature of ruthenium–nitrosyl complexes containing five π-acceptor pyridines in the metal coordination sphere.[13a]

The quantum yield of NO· release (ϕ_{NO}) observed for [**2**]$(PF_6)_3$ under 436 nm light irradiation is 0.01. This value is

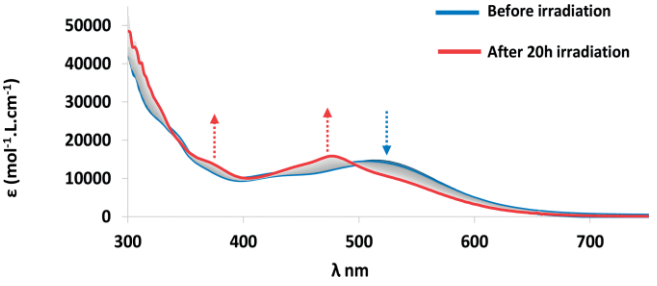

Figure 8. Evolution in the absorption spectra of [**2**]$(PF_6)_3$ in acetonitrile upon irradiation at $\lambda = 436$ nm.

significantly reduced compared with the value of 0.03 measured for [**1**]$(PF_6)_3$. The electronic transitions in the carbazole complex turn out to be less efficient with respect to NO· release (lower ϕ_{NO}) than those of the fluorene-terpyridine complex, although they are associated with a more sizeable ligand→Ru(NO) charge transfer. This observation raises the issue of the mechanism involved in the NO· release process and that of ϕ_{NO} versus σ_{TPA} optimization. This will be addressed in the next section.

Additional Considerations of ϕ_{NO} and σ_{TPA}

In the search for efficient NO· donors induced by two-photon excitation, it is important to bear in mind that the figure of merit is not the quantum yield of photorelease (ϕ_{NO}) or the molecular cross-section (σ_{TPA}), but rather the $\phi_{NO}\sigma_{TPA}$ product, the so-called "uncaging cross-section" of the photoinduced process. Therefore, the search for the best candidates requires both properties to be considered simultaneously. So far, very few estimations of photorelease (ϕ_{NO}) and TPA (σ_{TPA}) capabilities have been made for [Ru(terpy)(bipy)(NO)] complexes (Table 9). It is important to bear in mind that ϕ_{NO} is estimated for a one-photon process, whereas σ_{TPA} refers to a two-photon process. Nevertheless, ϕ_{NO} is the number of NO· generated divided by the number of excited states promoted. Clearly, the efficiency of the photoreaction [Ru(NO)] → [Ru] + (NO) does not consider the route by which the excited state [Ru(NO)]* is reached. Thus, one- and two-photon excitations lead to the same quantum yield.

Table 9. Parameters of interest for the two-photon-induced release of NO· (σ_{TPA} and ϕ_{NO}) from ruthenium–terpyridine-nitrosyl complexes.[a]

Compounds	ϕ_{NO}	σ_{TPA} [GM]	$\phi_{NO}\sigma_{TPA}$
[**1**]$(PF_6)_3$	0.06[b] (405)	108.0[b] (800)	6.5
	0.03 (436)		3.2
[**2**]$(PF_6)_3$	0.01 (436)	159.2 (800)	1.5

[a] The values in parentheses are the wavelengths of the incident irradiation (λ in nm). [a] Ref.[13a].

The data in Table 9 suggests that enhancing the σ_{TPA} value would lead to a lowering of ϕ_{NO} for this series of complexes, in contrast to our initial intuition that the efficiency of NO· release would reflect the strength of the charge transfer towards the nitrosyl.

In fact, the mechanism of the NO· release process is still controversial. Indeed, several reviews have discussed the dissocia-

tive mechanism of $M^{II}NO^{+}$ as resulting from photoinduced intramolecular electron transfer to NO^{+} and concomitant oxidation of the metal center to M^{III}. Then, the resulting $M^{III}NO\cdot$ species undergoes a "facile" NO· release.[6b,37] Therefore the presence of an electron-rich ligand should encourage this process. Nevertheless, the final cleavage of the Ru–NO bond remains unexplained within this picture, except by emphasizing the strong antibonding character of the d–π* overlap between the ruthenium and nitrogen atoms, which leads to a reduction of the bond order. On the other hand, we have recently observed that for a series of $[Ru^{II}(R\text{-terpy})(Cl)_2(NO)]^{+}$ complexes, there is no clear correlation between the donating/withdrawing character of R and the ϕ_{NO} values.[21] Furthermore, a recent theoretical investigation has suggested that the NO· release could require more than one photon with the contribution of an intermediate triplet state.[38] Altogether, these features tend to suggest that enhancing the donating capabilities of the ligands may not be the only fruitful strategy in this approach towards efficient NO· donors, which could also encompass molecules of greater complexity [e.g., polymetallic Ru(NO) complexes] than those envisioned in the initial stage of these investigations. We are currently exploring these possibilities.

Conclusions

In this research aimed at designing ruthenium–nitrosyl complexes with two-photon-induced NO· release capabilities we have observed that replacing a fluorenyl unit on a terpyridine ligand by a carbazole leads to a sizeable enhancement of the intramolecular push–pull properties from the substituted terpyridine to the withdrawing nitrosyl ligand, which can be evidenced by spectroscopic and electrochemical methods. The electronic features of the carbazole-substituted ligand leads to a higher TPA cross-section (σ_{TPA}) and lower quantum yield (ϕ_{NO}). The first experimental data available indicate that the two-photon encaging cross-section of the overall two-photon-induced NO· release ($\phi_{NO}\sigma_{TPA}$) is surprisingly less favorable within this series of $[Ru^{II}(terpy)(bipy)(NO)]^{3+}$ complexes when the donating capabilities of the ligands are more pronounced. Finding a definitive rationale to this observation is not straightforward. Electronic and structural features are both likely to play a role. Further investigations are currently under progress.

Experimental Section

Material and Equipment: 2-Acetylpyridine (Alfa-Aesar), carbazole (Sigma–Aldrich), iodoethane (Sigma–Aldrich), 2,2′-bipyridine (TCI), triethylamine (Sigma–Aldrich), *N*-bromosuccinimide (NBS, Sigma–Aldrich), lithium chloride (ACROS), sodium nitrite (Alfa-Aesar), lithium chloride (ACROS), NH_4PF_6 (Alfa-Aesar), $RuCl_3{\cdot}3H_2O$ (STREM), and *n*BuLi (1.6 M in hexanes; Sigma–Aldrich) were used without further purification. The solvents were analytical grade and used without further purification. Elemental analyses were performed at LCC with a Perkin–Elmer 2400 series II Instrument. ^{1}H NMR spectra were recorded with a Bruker Avance 300 or 400 spectrometer at 298 K in $CDCl_3$ or CD_3CN as internal reference. IR spectra were recorded with a Perkin–Elmer 1725 spectrometer. Electron paramagnetic resonance experiments (EPR) were performed with a Bruker ESP 500E spectrometer. The following settings were employed for the measurements: microwave power, 20 mW; field modulation amplitude, 0.1 mT; field modulation frequency, 100 kHz; microwave frequency, 9.782512 GHz. N-Methyl-D-glucamine dithiocarbamate previously synthetized reacted with Mohr salts to provide $[Fe(MGD)_2]$.[36] [**2**]$(PF_6)_3$ (90 μL of 1 mM solution in acetonitrile) was mixed with $[Fe(MGD)_2]$ (10 μL of a 2 mM aqueous solution) and injected into quartz capillaries. Samples were irradiated directly in the EPR cavity. The light source was a 250 W Oriel Hg lamp (Palaiseau, France). The light was passed through an Oriel WG 400 UV filter (λ > 400 nm; Palaiseau,France) and delivered through an optical fiber to the grid of the cavity.

Synthesis

3-Bromo-9*H*-carbazole (A): Carbazole (2 g, 11.96 mmol) was dissolved in DMF (25 mL), cooled to 0 °C, and covered with aluminium to protect it from the light. NBS (2.128 g, 11.96 mmol) was dissolved in DMF (25 mL) and added dropwise to the solution containing the carbazole, and the resulting mixture was allowed to warm to room temperature. The reaction mixture was left for 3 h and then poured into a mixture of ice/water (100 mL). The resulting solid was filtered under vacuum and then recrystallized from ethanol to give 2.20 g (8.97 mmol, 75 %) of a grey-pink solid (m.p. 199–200 °C).

3-Bromo-9-ethyl-9*H*-carbazole (B): Compound **A** (3 g, 12.19 mmol) and tetrabutylammonium iodide (300 mg) were placed in a flask and a solution of 50 % sodium hydroxide in water (25 mL) was added followed by ethyl iodide (2.92 mL, 36.5 mmol). The mixture was stirred vigorously at 30 °C for 24 h under nitrogen. The aqueous phase was then extracted with ethyl acetate (3 × 30 mL) and then dried with sodium sulfate and evaporated at reduced pressure. The solid obtained was then recrystallized from ethanol leading to 2.58 g (9.41 mmol, 77 %) of a white solid (m.p. 79–80 °C). ^{1}H NMR (300 MHz, $CDCl_3$): δ = 8.25 (dd, *J* = 2.0, 0.6 Hz, 1 H), 8.10 (ddd, *J* = 7.8, 1.2, 0.6 Hz, 1 H), 7.59 (dd, *J* = 8.7, 2.0 Hz, 1 H), 7.53 (dd, *J* = 7.0, 1.2 Hz, 1 H), 7.46 (dt, *J* = 8.3, 1.2 Hz, 1 H), 7.38–7.28 (m, 1 H), 7.33–7.23 (m, 1 H), 4.40 (q, *J* = 7.2 Hz, 2 H), 1.47 (t, *J* = 7.2 Hz, 3 H) ppm.

9-Ethyl-9*H*-carbazole-3-carbaldehyde (C): Compound **B** (2 g, 7.29 mmol) was placed in a flask, purged with nitrogen, diluted with dry THF (20 mL), and cooled to –74 °C. *n*BuLi (11 M in hexanes, 1.3 mL, 14.6 mmol) was added dropwise resulting in a yellow solution, which was kept at –74 °C for 1 h and then dry DMF (2.8 mL, 36.5 mmol) was added in one step. The reaction mixture was kept at –74 °C for 1 h and then conc. HCl (3 mL, ca. 36 mmol) was added in one step and the reaction mixture allowed to warm to room temperature and then left for 1 h. The reaction was diluted with water (20 mL) and extracted with ethyl acetate (3 × 30 mL). The organic phase was dried with sodium sulfate and then evaporated under reduced pressure. It was purified by silica gel column chromatography with hexane/ethyl acetate (9:1) as eluent to yield 1.23 g (5.54 mmol, 76 %) of a transparent oil. ^{1}H NMR (300 MHz, $CDCl_3$): δ = 10.14 (s, 1 H), 8.66 (dd, *J* = 1.6, 0.6 Hz, 1 H), 8.21 (ddd, *J* = 8.2, 1.2, 0.8 Hz, 1 H), 8.06 (dd, *J* = 8.6, 1.6 Hz, 1 H), 7.59 (ddd, *J* = 8.2, 7.0, 1.2 Hz, 1 H), 7.53 (d, *J* = 8.6 Hz, 1 H), 7.51 (dt, *J* = 8.2, 1.2 Hz, 1 H), 7.38 (ddd, *J* = 8.2, 7.0, 1.2 Hz, 1 H), 4.46 (q, *J* = 7.2 Hz, 2 H), 1.52 (t, *J* = 7.2 Hz, 3 H) ppm.

(*E*)-3-(9-Ethyl-9*H*-carbazol-3-yl)-1-(pyridin-2-yl)prop-2-en-1-one (D): Compound C (2.56 g, 11.46 mmol) was suspended in 96 % ethanol (100 mL) and then 2-acetylpyridine (1.3 mL, 11.46 mmol) was added. A solution containing sodium hydroxide (900 mg, 22.5 mmol) in water (25 mL) was added dropwise to the reaction mixture, which was stirred at room temperature for 24 h to give a

yellow solid. This solid was filtered under vacuum and then washed with water and cold ethanol to yield 3.4 g (10.4 mmol, 90 %) of the desired product. ^{1}H NMR (400 MHz, $CDCl_3$): δ = 8.78 (ddd, *J* = 4.8, 1.8, 0.9 Hz, 1 H), 8.46 (d, *J* = 1.8 Hz, 1 H), 8.35 (d, *J* = 15.9 Hz, 1 H), 8.27–8.23 (m, 1 H), 8.20 (d, *J* = 15.9 Hz, 1 H), 8.14 (d, *J* = 7.7 Hz, 1 H), 7.89–7.83 (m, 2 H), 7.53–7.44 (m, 2 H), 7.39 (t, *J* = 8.3 Hz, 2 H), 7.33–7.24 (m, 1 H), 4.33 (q, *J* = 7.2 Hz, 2 H), 1.43 (t, *J* = 7.2 Hz, 3 H) ppm.

4′-(*N*-Ethyl-9*H*-carbazol-3-yl)-2,2′:6′,2″-terpyridine (E): A mixture of compound **D** (1 g, 3 mmol), 1-(2-oxo-2-pyridin-2-ylethyl)pyridinium iodide (1.0 g, 3 mmol), and ammonium acetate (2.36 g, 30 mmol) was suspended in ethanol (50 mL) and heated at reflux for 20 h. After cooling to room temperature, the resulting green solid was filtered under vacuum and purified by silica gel column chromatography with a mixture of hexane/acetone (8:2) as eluent to yield 392 mg (9.19 mmol, 30 %) of the resulting ligand as a yellow solid. ^{1}H NMR (400 MHz, $CDCl_3$): δ = 8.87 (s, 2 H), 8.77 (dd, *J* = 4.7, 0.8 Hz, 2 H), 8.70 (d, *J* = 8.0 Hz, 2 H), 8.67 (d, *J* = 1.6 Hz, 1 H), 8.23 (d, *J* = 7.7 Hz, 1 H), 8.05 (dd, *J* = 8.5, 1.8 Hz, 1 H), 7.88 (td, *J* = 7.7, 1.8 Hz, 2 H), 7.53–7.49 (m, 1 H), 7.49–7.47 (m, 1 H), 7.43 (d, *J* = 8.1 Hz, 1 H), 7.35 (ddd, *J* = 7.4, 4.8, 1.0 Hz, 2 H), 7.32–7.26 (m, 1 H), 4.40 (q, *J* = 7.2 Hz, 2 H), 1.47 (t, *J* = 7.2 Hz, 3 H) ppm.

[Ru^{III}Cl$_3$(E)] (F): The ligand **E** (150 mg, 0.35 mmol) was suspended with $RuCl_3 \cdot H_2O$ (92 mg, 0.35 mmol) in ethanol (25 mL). The reaction mixture was protected from the light and heated at reflux for 3 h. It was then allowed to cool to room temperature and subsequently cooled with ice. The resulting solid was filtered under vacuum and rinsed with ethanol and diethyl ether to yield 212 mg (0.33 mmol, 95 %) of a dark-brown powder.

[Ru^{II}(bipy)(Cl)(E)](Cl) (G): A mixture of complex **F** (100 mg, 0.158 mmol), 2,2′-bipyridine (2.25 mg, 0.158 mmol), LiCl (40 mg, 0.946 mmol), and triethylamine (0.1 mL) was added to a flask and suspended in 75 % ethanol (20 mL). The reaction mixture was protected from the light and heated at reflux for 4 h. Then it was then allowed to cool to room temperature and subsequently cooled with ice. The resulting solid was filtered under vacuum and rinsed with water, ethanol, and diethyl ether to yield 100 mg (0.134 mmol, 85 %) of a purple solid. ^{1}H NMR (300 MHz, CD_3CN): δ = 10.28 (d, *J* = 5.6 Hz, 1 H), 9.20 (s, 1 H), 9.03 (s, 2 H), 8.67–8.53 (m, 3 H), 8.42 (d, *J* = 7.8 Hz, 1 H), 8.37–8.24 (m, 3 H), 7.98 (ddd, *J* = 7.4, 5.7, 1.3 Hz, 1 H), 7.88–7.76 (m, 3 H), 7.74–7.62 (m, 4 H), 7.60–7.53 (m, 1 H), 7.45 (d, *J* = 5.8 Hz, 1 H), 7.32 (t, *J* = 7.3 Hz, 1 H), 7.28–7.17 (m, 1 H), 6.99 (ddd, *J* = 7.4, 5.8, 1.3 Hz, 2 H), 4.55 (q, *J* = 7.2 Hz, 2 H), 1.50 (t, *J* = 7.2 Hz, 3 H) ppm.

[Ru^{II}(bipy)(E)(NO$_2$)](PF$_6$) (H): A mixture of complex **G** (155 mg, 0.205 mmol) and $NaNO_2$ (142 mg, 2.05 mmol) was suspended in 75 % ethanol (20 mL). The reaction mixture was protected from the light and heated at reflux for 4 h. It was then allowed to cool to room temperature and subsequently cooled with ice. NH_4PF_6 (100 mg, 0.61 mmol) dissolved in water (3 mL) was added to the reaction mixture, upon which a red precipitate appeared. This was filtered under vacuum and then rinsed with water, ethanol, and diethyl ether to yield 122 mg (0.679 mmol, 70 %) of the desired complex **H** as a red solid. FTIR (ATR): $\tilde{\nu}$ = 1295 (νNO_2) cm^{-1}. ^{1}H NMR (400 MHz, CD_3CN): δ = 9.95 (dd, *J* = 5.5, 1.3 Hz, 1 H), 8.95 (d, *J* = 1.9 Hz, 1 H), 8.84 (s, 2 H), 8.61 (d, *J* = 8.2 Hz, 1 H), 8.49 (d, *J* = 7.9 Hz, 2 H), 8.38 (d, *J* = 8.0 Hz, 1 H), 8.30 (dd, *J* = 7.8, 1.4 Hz, 2 H), 8.27–8.21 (m, 1 H), 7.99 (ddd, *J* = 7.4, 5.6, 1.3 Hz, 1 H), 7.92 (td, *J* = 7.9, 1.6 Hz, 2 H), 7.82 (d, *J* = 8.7 Hz, 2 H), 7.78 (d, *J* = 4.9 Hz, 2 H), 7.68 (d, *J* = 8.3 Hz, 1 H), 7.61 (ddd, *J* = 8.3, 7.0, 1.2 Hz, 1 H), 7.47 (d, *J* = 5.7 Hz, 1 H), 7.36 (ddd, *J* = 8.0, 7.0, 1.0 Hz, 1 H), 7.31 (ddd, *J* = 7.7, 5.5, 1.3 Hz, 2 H), 7.08 (ddd, *J* = 7.3, 5.6, 1.2 Hz, 1 H), 4.58 (q, *J* = 7.2 Hz, 2 H), 1.52 (t, *J* = 7.2 Hz, 3 H) ppm.

[Ru^{II}(bipy)(E)(NO)](PF$_6$)$_3$ ([2](PF$_6$)$_3$): A mixture of ethanol (15 mL) and conc. HCl (4 mL, ca. 50 mmol) was added to complex **H** (34 mg, 38.86 μmol). The reaction was protected from the light and heated at 60 °C for 2 h. After cooling down with ice, NH_4PF_6 (100 mg, 0.61 mmol) dissolved in water (3 mL) was added to the reaction mixture, which led to a purple precipitate. This was filtered under vacuum and then rinsed with water, ethanol, and diethyl ether to yield 31 mg (26.9 μmol, 70 %) of a purple solid. FTIR (ATR): $\tilde{\nu}$ = 1937 (νNO) cm^{-1}. UV/Vis: λ_{max} (ε) = 517 nm (14600 L mol^{-1} cm^{-1}). ^{1}H NMR (400 MHz, CD_3CN): δ = 9.35 (d, *J* = 5.5 Hz, 1 H), 9.23 (s, 2 H), 9.21 (d, *J* = 2.0 Hz, 1 H), 8.95 (dd, *J* = 8.2, 0.9 Hz, 2 H), 8.84 (d, *J* = 8.2 Hz, 1 H), 8.73 (td, *J* = 8.0, 1.4 Hz, 1 H), 8.65 (d, *J* = 8.3 Hz, 1 H), 8.53 (td, *J* = 7.9, 1.5 Hz, 2 H), 8.45 (dd, *J* = 8.8, 2.1 Hz, 1 H), 8.42 (d, *J* = 8.2 Hz, 1 H), 8.35–8.26 (m, 2 H), 8.07–8.03 (m, 2 H), 7.93 (d, *J* = 8.8 Hz, 1 H), 7.77–7.72 (m, 3 H), 7.70–7.65 (m, 1 H), 7.54 (ddd, *J* = 7.5, 6.0, 1.3 Hz, 1 H), 7.49–7.44 (m, 1 H), 7.43–7.41 (m, 1 H), 4.60 (q, *J* = 7.2 Hz, 2 H), 1.53 (t, *J* = 7.2 Hz, 3 H) ppm. $C_{39}H_{30}F_{18}N_7OP_3Ru$ (1148.67): calcd. C 40.78, H 2.63, N 8.54; found C 40.17, H 2.45, N 8.25.

Crystallographic Data: The crystal data of **H** were collected at low temperature [100(2) K] with a Bruker Kappa Apex II diffractometer equipped with a 30 W air-cooled microfocus using Mo-K_α radiation (λ = 0.71073 Å) and an Oxford Cryosystems Cryostream cooler device. ϕ and ω scans were used for data collection. The structure was solved by the intrinsic phasing method (SHELXT).[39] All non-hydrogen atoms were refined anisotropically by means of least-squares procedures on F^2 with the aid of the SHELXL program.[40] All the hydrogen atoms were refined isotropically at calculated positions by using a riding model. The crystal structure with only NO_2 coordinated to the Ru atom was not fully acceptable; anisotropic displacement parameters and the residual electron density suggested a disorder between the NO_2 group and a Cl atom in a ratio 90:10 after refinement.

CCDC 1564051 (for **H**) contains the supplementary crystallographic data for this paper. These data can be obtained free of charge from The Cambridge Crystallographic Data Centre.

Computational Studies: The ruthenium complexes [**1**]$^{3+}$, [**2**]$^{3+}$, [**1′**]$^{3+}$, and [**2′**]$^{3+}$ were optimized in the gas phase by using the Gaussian 09 program package[41] within the framework of DFT. The double-ζ basis set 6-31G* was used for all atoms except the heavy ruthenium atom, for which the LANL2DZ basis set was applied to account for relativistic effects.[42] The two hexyl chains present in [**1**]$^{3+}$ and [**1′**]$^{3+}$ were replaced by two methyl groups to help the convergence process. To be consistent with our previous report,[13c] and in agreement with a previous investigation of ruthenium–nitrosyl by Rose and Mascharak,[43] we selected the hybrid functional B3PW91 for the optimization. The B3PW91 functional has been shown to outperform other hybrid functionals (e.g., B3LYP) and pure functionals (e.g., PW91) in numerous cases of ruthenium complexes, especially when back-bonding ligands (like NO) are present.[43,44] The vibrational analyses were performed at the same level of theory to verify that the stationary points correspond to minima on the potential energy surfaces. The UV/Vis electronic spectra were then computed at the CAM-B3LYP/6-31G* level of theory, which was selected for its good efficiency in reproducing experimental transition energies. Solvent effects were included by using the polarizable continuum model (PCM) implemented in Gaussian 09 for acetonitrile (ε = 35.688). Molecular orbitals were plotted with GABEDIT 2.4.8.[45] The optimized geometries are provided in Supporting Information.

Electrochemistry: Electrochemical experiments were performed at room temperature in a homemade air-tight three-electrode cell connected to a vacuum/argon line. The reference electrode was a saturated calomel electrode (SCE) separated from the solution by a bridge compartment, the counter electrode was a platinum wire with an apparent surface area of around 1 cm^2, and the working electrode was a Pt microdisk (radius = 0.25 mm). The supporting electrolyte, (nBu$_4$N)(PF$_6$) (Fluka, 99 % electrochemical grade), was used as received and simply degassed under argon. Acetonitrile was freshly purified prior to use. The concentrations of solutions used during the electrochemical studies were typically 10^{-3} and 10^{-1} mol L^{-1} in supporting electrolyte. Before each measurement, the solutions were degassed by bubbling argon through them, and the working electrode was polished with a polishing machine (Presi P230).

Z-Scan Measurements: The Z-scan technique[46] was used to measure the nonlinear absorption coefficients of the samples at 800 nm by using short laser pulses of 350 fs at 1 kHz repetition rate. The compounds under study were dissolved in acetonitrile at the concentration of 1×10^{-2} mol L^{-1}. Z-scan traces for each solution were measured at different energies (180, 250, 360, and 460 nJ per pulse) The samples were measured at least four times at each energy. To verify the validity of our measurements, the same Z-scan apparatus was first used to measure in the close aperture approach the nonlinear refractive index n_2 of the standard CS_2. The results led to n_2 values in the range (1–2) $\times 10^{-15}$ cm^2 W^{-1}, which is in very good agreement with the values accepted for this standard reference. Then the laser dye rhodamine B (RB; dissolved in methanol at the concentration of 1×10^{-2} mol L^{-1}) was measured for comparison of σ_{TPA}, along with the sample tested in the open aperture approach. In this case, the value of σ_{TPA} of RB was found equal to 104 ± 12 (for a pulse of 350 fs), also in very good agreement with the value accepted in the literature (reference value 120 GM).[47] The nonlinear absorption coefficient β of each sample was obtained after fitting the normalized transmission $T(z)$ to the Z-scan formalism. A total of 25 plots of Z-scans were analyzed. The TPA cross-section (σ_{TPA}) was obtained from Equation (2), in which N is the molecular density and ω is the optical frequency.

$$\sigma_{TPA} = \frac{\hbar\omega}{N}\beta \quad (2)$$

Photochemistry: Kinetic studies on the photolysis reactions were carried out with a diode array Hewlett–Packard 8454A spectrophotometer. Solutions of 3 mL of [**1**](PF$_6$)$_3$ (5.35×10^{-5} mol L^{-1}) and [**2**](PF$_6$)$_3$ (7.35×10^{-5} mol L^{-1}) in non-deoxygenated acetonitrile were used. The optical fiber was fixed laterally on the cuvette. Absorption spectra were recorded after each minute, in fast scan mode, during a period of 7 h for both complexes, which allowed apparently stable absorption conditions to be reached. The UV/Vis spectra were recorded under irradiation realized with a Muller reactor device equipped with a cooling water filter and a mercury arc lamp equipped with an appropriate interference filter to isolate the desired irradiation wavelength (λ_{max} = 436 nm, intensity 8 mW). The light intensity was determined by using a ferrioxalate actinometer. The sample solutions were placed in a quartz cuvette of 1 cm path length stirred continuously. The temperature was maintained at 27 °C during the whole experiment.

Quantum Yield Measurements: Light intensities were determined before each photolysis experiment by chemical actinometry procedures. The actinometers used were potassium ferrioxalate for λ_{irr} = 436 nm [$I_0 = 1.01 \times 10^{-6}$ mol L^{-1} s^{-1} for [**1**](PF$_6$)$_3$ and $I_0 = 8.13 \times 10^{-7}$ mol L^{-1} s^{-1} for [**2**](PF$_6$)$_3$]. The quantum yields (ϕ_A) were determined by using the Sa3.3 program written by Lavabre and Pimienta,[48] which allows the resolution of the differential Equation (3).

$$\frac{d[A]}{dt} = -\phi_A I_a^A = -\phi_A \mathrm{Abs}_A^{\lambda} I_0 F \quad (3)$$

in which I_a^A is the intensity of the light absorbed by the precursor, Abs_A^{λ} is the absorbance of [**1**]$^{3+}$ or [**2**]$^{3+}$ before irradiation, I_0 is the incident intensity measured at 436 nm, and F is the photokinetic factor given by Equation (4).

$$F = \frac{(1-10^{-\mathrm{Abs}_{Tot}^{\lambda}})}{\mathrm{Abs}_{Tot}^{\lambda}} \quad (4)$$

in which $\mathrm{Abs}_{Tot}^{\lambda}$ is the total absorbance. Equation (3) was fitted with the experimental data $\mathrm{Abs}_{Tot}^{\lambda} = f(t)$ and the parameters ϕ_A and ε_B (ε_B is the molar extinction coefficient measured at the end of the reaction) at two wavelengths (λ_{irr} = 436 nm and λ_{obs} = 470 nm for [**1**]$^{3+}$ and 550 nm for [**2**]$^{3+}$). λ_{obs} was chosen because it corresponds to a large difference between molar extinction coefficient at the beginning and end of the photochemical reaction. Simulation and optimization procedures were performed by using numerical integration and a nonlinear minimization algorithm for the fitting of the model to the experimental data.[48,49]

[**1**]$^{3+}$

$[A]_0 = 5.35\ 10^{-5}\mathrm{mol.\ L^{-1}}, \varepsilon_A^{436} = 15514\ \mathrm{mol^{-1}.\ L.\ cm^{-1}}, \varepsilon_A^{470} = 15204\ \mathrm{mol^{-1}.\ L.\ cm^{-1}}$,
$\varepsilon_B^{436} = 14349\ \mathrm{mol^{-1}.\ L.\ cm^{-1}}, \varepsilon_B^{470} = 22019\ \mathrm{mol^{-1}.\ L.\ cm^{-1}}$

[**2**]$^{3+}$

$[A]_0 = 7.35\ 10^{-5}\mathrm{mol.\ L^{-1}}, \varepsilon_A^{436} = 11292\ \mathrm{mol^{-1}.\ L.\ cm^{-1}}, \varepsilon_A^{550} = 11931\ \mathrm{mol^{-1}.\ L.\ cm^{-1}}$,
$\varepsilon_B^{436} = 12106\ \mathrm{mol^{-1}.\ L.\ cm^{-1}}, \varepsilon_B^{550} = 8187\ \mathrm{mol^{-1}.\ L.\ cm^{-1}}$

Supporting Information (see footnote on the first page of this article): Crystal data, DFT geometries, voltammograms for [**1**](PF$_6$)$_3$ and [**2**](PF$_6$)$_3$, and changes in absorption spectra for [**1**](PF$_6$)$_3$.

Acknowledgments

This work was performed within the framework of the French-Mexican International Laboratory (LIA-LCMMC). The authors thank the Centre National de la Recherche Scientifique (CNRS, France) and CONACyT (México) for financial support, Marine Tassé for recording the photorelease properties, and Dr. Alix Sournia-Saquet for the electrochemical measurements. A. E. C. thanks CONACyT for a Ph. D. fellowship (270200).

Keywords: Ruthenium · Nitrogen oxides · Drug delivery · Density functional calculations · Photochemistry · Electronic structure · Charge transfer

[1] a) B. Bonavida (Ed.), *Nitric Oxide and Cancer: Prognosis, Prevention and Therapy*, Springer, New York, **2010**; b) L. J. Ignarro (Ed.), *Nitric Oxide: Biology and Pathology*, Academic Press, San Diego, CA, **2000**.
[2] S. Singh, A. K. Gupta, *Cancer Chemother. Pharmacol.* **2011**, *67*, 1211.
[3] D. A. Wink, L. A. Ridnour, S. P. Hussain, C. C. Harris, *Nitric Oxide* **2008**, *19*, 65–67.
[4] M. J. Rose, P. K. Mascharak, *Curr. Opin. Chem. Biol.* **2008**, *12*, 238.
[5] M. G. Spey, K. M. Miranda, D. D. Thomas, S. Xavier, D. Citrin, M. P. Vitek, D. A. Wink, *Ann. N. Y. Acad. Sci.* **2006**, *962*, 195–206.

[6] a) N. L. Fry, P. K. Mascharak, *Acc. Chem. Res.* **2011**, *44*, 289–298; b) M. J. Rose, P. K. Mascharak, *Coord. Chem. Rev.* **2008**, *252*, 2093–2114.
[7] M. Pawlicki, H. A. Collins, R. G. Denning, H. L. Anderson, *Angew. Chem. Int. Ed.* **2009**, *48*, 3244–3266; *Angew. Chem.* **2009**, *121*, 3292.
[8] C. Andraud, R. Fortrie, C. Barsu, O. Stéphan, H. Chermette, P. L. Baldeck, *Adv. Polym. Sci.* **2008**, *214*, 149–203.
[9] G. S. He, L. S. Tan, Q. Zheng, P. N. Prasad, *Chem. Rev.* **2008**, *108*, 1245–1330.
[10] F. Terenziani, C. Katan, E. Badaeva, S. Tretiak, M. Blanchard-Desce, *Adv. Mater.* **2008**, *20*, 4641–4678.
[11] B. Strehmel, V. Strehmel, *Adv. Photochem.* **2007**, *33*, 111–341.
[12] M. R. Hamblin, T. N. Demidova, *Proc. SPIE, Mechanism for Low-Light Therapy* **2006**, *6140*, 614001–614012.
[13] a) A. Enriquez-Cabrera, I. Sasaki, V. Bukhanko, M. Tassé, S. Mallet-Ladeira, P. G. Lacroix, R. M. Barba-Barba, G. Ramos, N. Farfán, Z. Voitenko, I. Malfant, *Eur. J. Inorg. Chem.* **2017**, 1446–1456; b) J. Akl, I. Sasaki, P. G. Lacroix, V. Hugues, M. Bocé, S. Mallet-Ladeira, P. Vicendo, M. Blanchard Desce, I. Malfant, *Photochem. Photobiol. Sci.* **2016**, *15*, 1484–1491; c) J. Akl, I. Sasaki, P. G. Lacroix, I. Malfant, S. Mallet-Ladeira, P. Vicendo, N. Farfán, R. Santillan, *Dalton Trans.* **2014**, *43*, 12721–12733.
[14] a) R. Kannan, G. S. He, L. Yuan, F. Xu, P. N. Prasad, A. G. Dombroskie, B. A. Reinhardt, J. W. Baur, R. A. Vaia, L. S. Tan, *Chem. Mater.* **2001**, *13*, 1896–1904; b) R. Kannan, G. S. He, T. C. Lin, P. N. Prasad, R. A. Vaia, L. S. Tan, *Chem. Mater.* **2004**, *16*, 185–194; c) Q. Zheng, G. S. He, P. N. Prasad, *Chem. Mater.* **2005**, *17*, 6004–6011; d) T. C. Lin, G. S. He, Q. Zheng, P. N. Prasad, *J. Mater. Chem.* **2006**, *16*, 2490–2498.
[15] a) O. Mongin, L. Porrès, C. Katan, T. Pons, J. Mertz, M. Blanchard-Desce, *Tetrahedron Lett.* **2003**, *44*, 8121–8125; b) C. Le Droumaguet, O. Mongin, M. H. V. Werts, M. Blanchard-Desce, *Chem. Commun.* **2005**, 2802–2804; c) O. Mongin, X. Yan, L. Porrès, M. Charlot, C. Katan, M. Blanchard-Desce, *Chem. Eur. J.* **2007**, *13*, 1481–1498.
[16] a) M. Halik, W. Wenseleers, C. Grasso, F. Stellacci, E. Zojer, S. Barlow, J. L. Bredas, J. W. Perry, S. R. Marder, *Chem. Commun.* **2003**, 1490–1491.
[17] a) K. D. Belfield, A. R. Morales, B. S. Kang, J. M. Hales, D. J. Hagan, E. W. VanStryland, V. M. Chapela, J. Percino, *Chem. Mater.* **2004**, *16*, 4634–4661; b) K. D. Belfield, A. R. Morales, J. M. Hales, D. J. Hagan, E. W. Van Stryland, V. M. Chapela, J. Percino, *Chem. Mater.* **2004**, *16*, 2267–2273; c) S. Yao, K. D. Belfield, *J. Org. Chem.* **2005**, *70*, 5126–5132.
[18] C. Kong, M. Peng, H. Shen, Y. Wang, Q. Zhang, H. Wang, J. Zhang, H. Zhou, J. Yang, J. Wu, Y. Tian, *Dyes Pigm.* **2015**, *120*, 328–334.
[19] G. Saikia, P. K. Iyer, *J. Org. Chem.* **2010**, *75*, 2714–2717.
[20] H. Huang, Q. Fu, B. Pan, S. Zhuang, L. Wang, J. Chen, D. Ma, C. Yang, *Org. Lett.* **2012**, *14*, 4786–4789.
[21] S. Amabilino, M. Tassé, P. G. Lacroix, S. Mallet-Ladeira, V. Pimienta, J. Akl, I. Sasaki, I. Malfant, *New J. Chem.* **2017**, *41*, 7371–7383.
[22] P. De, B. Sarkar, S. Maji, A. K. Das, E. Bulak, S. M. Mobin, W. Kaim, G. G. Lahiri, *Eur. J. Inorg. Chem.* **2009**, 2702–2710.
[23] K. Karidi, A. Garoufis, N. Hadjiliadis, M. Lutz, A. L. Spek, J. Reedijk, *Inorg. Chem.* **2006**, *45*, 10282–10292.
[24] G. Nakamura, M. Kondo, M. Crisalli, S. Koon Lee, A. Shibata, P. C. Ford, S. Masaoka, *Dalton Trans.* **2015**, *44*, 17189–17200.
[25] N. Chanda, D. Paul, S. Kar, S. M. Mobin, A. Datta, V. G. Puranik, K. K. Rao, G. K. Lahiri, *Inorg. Chem.* **2005**, *44*, 3499–3511.
[26] R. Chauvin, Ch. Lepetit, *Phys. Chem. Chem. Phys.* **2013**, *15*, 3855–3830, and references cited therein.
[27] D. R. Lang, J. A. Davis, L. G. F. Lopes, A. A. Ferro, L. C. G. Vasconcellos, D. W. Franco, E. Tfouni, A. Wieraszko, M. J. Clarke, *Inorg. Chem.* **2000**, *39*, 2294–2300.
[28] H. Nagao, K. Enomoto, Y. Wakabayashi, G. Komiya, T. Hirano, T. Oi, *Inorg. Chem.* **2007**, *46*, 1431–1439.
[29] K. Karidi, A. Garoufis, A. Tsipis, N. Hadjiliadis, H. den Dulk, J. Reedijk, *Dalton Trans.* **2005**, 1176–1187.
[30] A. D. Laurent, D. Jacquemin, *Int. J. Quant. Mech.* **2013**, *113*, 2019–2039.
[31] W. R. Murphy Jr., K. Takeuchi, M. H. Barley, T. J. Meyer, *Inorg. Chem.* **1986**, *25*, 1041–1053.
[32] See ref.[22]
[33] S. Maji, B. Sarkar, M. Patra, A. K. Das, S. M. Mobin, W. Kaim, G. K. Lahiri, *Inorg. Chem.* **2008**, *47*, 3218–3227.
[34] E. W. Van Stryland, M. Sheik-Bahae in *Characterization Techniques and Tabulations for Organic Nonlinear Materials* (Eds.: M. G. Kuzyk, C. W. Dirk), Marcel Dekker, New York, **1998**, pp. 655–682.
[35] A. F. Vanin, A. P. Poltorakov, V. D. Mikoyan, L. N. Kubrina, E. van Faassen, *Nitric Oxide* **2006**, *15*, 295–311.
[36] A. J. Liu, Q. Duan, J. Wang, Z. Song, X. Qiao, H. Wang, *J. Biomed. Opt.* **2015**, *20*, 015004-1–7.
[37] F. Roncaroli, M. Videla, L. D. Slep, J. A. Olabe, *Coord. Chem. Rev.* **2007**, *251*, 1903–1930.
[38] J. S. Garcia, F. Talotta, F. Alary, M. Dixon, M. Boggio-Pasqua, J. L. Heully, *J. Mol. Model.* **2016**, *22*, 1–10.
[39] G. M. Sheldrick, *Acta Crystallogr., Sect. A* **2015**, *71*, 3–8.
[40] G. M. Sheldrick, *Acta Crystallogr., Sect. A* **2008**, *64*, 112–122.
[41] M. J. Frisch, G. W. Trucks, H. B. Schlegel, G. E. Scuseria, M. A. Robb, J. R. Cheeseman, G. Scalmani, V. Barone, B. Mennucci, G. A. Petersson, H. Nakatsuji, M. Caricato, X. Li, H. P. Hratchian, A. F. Izmaylov, J. Bloino, G. Zheng, J. L. Sonnenberg, M. Hada, M. Ehara, K. Toyota, R. Fukuda, J. Hasegawa, M. Ishida, T. Nakajima, Y. Honda, O. Kitao, H. Nakai, T. Vreven, J. A. Montgomery Jr., J. E. Peralta, F. Ogliaro, M. Bearpark, J. J. Heyd, E. Brothers, K. N. Kudin, V. N. Staroverov, R. Kobayashi, J. Normand, K. Raghavachari, A. Rendell, J. C. Burant, S. S. Iyengar, J. Tomasi, M. Cossi, N. Rega, J. M. Millam, M. Klene, J. E. Knox, J. B. Cross, V. Bakken, C. Adamo, J. Jaramillo, R. Gomperts, R. E. Stratmann, O. Yazyev, A. J. Austin, R. Cammi, C. Pomelli, J. W. Ochterski, R. L. Martin, K. Morokuma, V. G. Zakrzewski, G. A. Voth, P. Salvador, J. J. Dannenberg, S. Dapprich, A. D. Daniels, Ö. Farkas, J. B. Foresman, J. V. Ortiz, J. Cioslowski, D. J. Fox, *Gaussian 09, Revision E.01*, Gaussian, Inc., Wallingford, CT, **2009**.
[42] a) P. J. Hay, W. R. Wadt, *J. Chem. Phys.* **1985**, *82*, 270–283; b) W. R. Wadt, P. J. Hay, *J. Chem. Phys.* **1985**, *82*, 284–298; c) P. J. Hay, W. R. Wadt, *J. Chem. Phys.* **1985**, *82*, 299–310.
[43] M. J. Rose, P. K. Mascharak, *Inorg. Chem.* **2009**, *48*, 6904–6917.
[44] P. Hirva, M. Haukka, M. Jaconen, *J. Mol. Model.* **2008**, *14*, 171–181.
[45] http://sites.Google.com/site/allouchear/Home/gabedit.
[46] See ref.[34]
[47] M. Kauert, P. C. Stoller, M. Frenz, J. Rička, *Opt. Express* **2006**, *14*, 8434–8447.
[48] D. Lavabre, V. Pimienta, *Program Sa3.3*, Cinet.Chim, Toulouse, **2010** (http://cinet.chim.pagesperso-orange.fr/tele_sa/install_Sa.html).
[49] V. Pimienta, C. Frouté, M.-H. Deniel, D. Lavabre, R. Guglielmetti, J. C. Micheau, *J. Photochem. Photobiol. A* **1999**, *122*, 199–204 (ref.[35]).

Received: July 24, 2017